Individualized modeling for the peripheral optics of the human myopic eye

Juan Tabernero,[1,*] Enian Kallamata,[2] Gabriella Velonias,[2] and Fuensanta A. Vera-Diaz[2]

[1]*Departamento de Electromagnetismo y Electrónica, Universidad de Murcia, Campus de Espinardo, Murcia, 30100, Spain*
[2]*New England College of Optometry, 424 Beacon Street, Boston, MA 02140, USA*
*juant@um.es

Abstract: Individualized optical modelling of the eye is a useful tool to estimate optical properties of the eye from a set of geometrical parameters. In the context of myopia research, it is important to understand not only the on-axis (foveal) optical quality, but also the peripheral profile. This work describes a method to extend on-axis individualized eye modeling to the peripheral retina. Using measurements of corneal geometry, axial distances, and central optical quality from a group of young adults, a crystalline lens model was built to help reproduce the peripheral optical quality of the eye. Subsequent individualized eye models were generated from each of the 25 participants. These models were used to predict the individual peripheral optical quality over the central 40 degrees. Outcomes of the final model were then compared to the actual measurements of peripheral optical quality in these participants, measured with a scanning aberrometer. A high agreement was found between the final model and measured optical quality for the relative spherical equivalent and J0 astigmatism.

1. Introduction

The aim of ocular modelling is to predict the standard optical properties of the human eye from a set of surfaces and refractive indexes that recreate the average geometry of the eye. The optical properties of the complete system of surfaces and indexes can then be obtained using paraxial ray-tracing methods [1–5] or with more sophisticated methods, such as those that solve the Snell law at the interface of rays with each surface [6–16].

Early eye models (paraxial models) were able to determine average central optical properties of the eye. The object would be aligned with the optical axis of the eye model and the physical extension of the object only subtended a few minutes of arc with respect to the axis. In these models, the image was well formed on the foveal (central) area. However, more complex eye models that solve the Snell law can be used to additionally explain peripheral optical properties of the eye. To create such models, the geometry of the retina is first required [17], over which it may be possible to fit other (unknown) ocular geometrical parameters to the experimental measurements [9,15,18,19] and solve the inverse problem.

Modelling the peripheral optical properties of the eye is of high relevance in the context of myopia research, as the peripheral retina plays a significant role in the development of myopia [20–22]. It has been hypothesized that imposing a modified optical image into the peripheral retina of the eye may have the capability to stop the progression of central foveal myopia [23,24]. Spectacles and contact lenses with modified peripheral optical properties have been accordingly designed [25–27], and specific *average* eye models for the myopic eye and retina have been proposed [28].

Individualized eye models [29] complement traditional eye modelling by obtaining individual predictions for each particular subject from a simple set of measurements. Typically, this modelling procedure needs measuring the maximum number of geometrical parameters available

with the existing ophthalmic instrumentation at the lab or clinic. A validation process of the predictions is required, whereby the outcome of the model is compared with the real measurements. An example of this procedure is the prediction of the optical quality of the eye after the implantation of an intraocular lens to replace the natural crystalline lens (cataract surgery) [30,31]. This model was simply based on measuring corneal topography, axial distances of the eye, and misalignments (tilt and decentration) of the IOL with respect to the visual axes. Tabernero et al. verified this model by measuring the wavefront (foveal) error of each subject and comparing it to the individual predictions [30].

This work is an extension of the previous modelling procedure by Tabernero et al. to the periphery of the eye, exploring how accurate a personalized model of the human eye in the periphery can be. One that is based on the least and simplest possible measurements taken with instrumentation available to clinicians [30]. This extension requires solving two more complications with respect to the previous (on-axis) modelling: i) the need for a crystalline lens model reproducing central *and peripheral* optical properties of the lens, and ii) the need of accurate instrumentation to measure peripheral properties of the eye (retinal geometry and peripheral wavefront error). These two questions and the re-formulation of the model for the periphery are developed in the sections to follow.

2. Methods

2.1. Instrumentation and measurements

Peripheral aberrations, corneal shape, and retinal shape were measured using a peripheral scanning Hartmann-Shack wavefront sensor (Voptica SL, Murcia, Spain), a Scheimpflug camera to image the anterior segment (Pentacam, Oculus, Germany), and an optical biometer based on partial coherence interferometry (Lenstar, Haag-Streit AG, Switzerland), respectively.

The peripheral scanning aberrometer is an open field Hartmann-Shack wavefront sensor mounted on a scanning arm that rotates quickly to measure aberrations over a horizontal central field of ±40° in less than two seconds. The angular resolution of the system is one degree. Technical details of the instrument are described elsewhere [32,33]. In this work, all calculations used a pupil diameter of 4 mm. Off-axis elliptical pupils were trimmed to fit the small spherical pupil in the ellipse. Fifth order Zernike polynomials were used to expand wavefront aberrations. Mean data from a total of five horizontal scans was used in this study. On average, at 20 degrees temporal field, the mean standard deviation of peripheral defocus obtained from the five scans was 0.24 ± 0.09 D. The same parameter for astigmatism (J0) was 0.16 ± 0.08 D and for coma (Z8) was 0.05 ± 0.03 μm.

The Pentacam device is a rotating Scheimpflug camera that allows measuring the anterior and posterior corneal surface 3D geometry, reconstructed from 100 Scheimpflug images (corneal meridians images taken every 1.8 degrees) [34].

The optical biometer, Lenstar, uses partial coherence interferometry to measure axial length (AXL) of the eye [35]. In order to obtain the profile for each retina, we measured the AXL on-axis and for 12 off-axis locations across the horizontal ±60°. A fixation non-accommodative target with small stars located at $\pm 30°$, $\pm 20°$, $\pm 16°$, $\pm 12°$, $\pm 8°$, $\pm 4°$ and 0° along the horizontal meridian was used to obtain the central and peripheral measurements. These angles and the corresponding AXL measured at each location were converted into retinal coordinates (a radial coordinate and a z-height) using Verkicharla et al. geometrical equations (stage 1 procedure) [35]. These equations were further individualized using the corneal radius measured for each subject with the Pentacam corneal topographer.

2.2. Modelling

Zemax Optics Studio 17.5 optical design software was used to model all the ocular surfaces. Corneal surfaces (anterior and posterior) were incorporated into the model as two biconic surfaces whose sag z-coordinate ("elevation") follows the equation:

$$z(x, y) = \frac{c_x x^2 + c_y y^2}{1 + \sqrt{1 - (1 + k_x)c_x^2 x^2 - (1 + k_y)c_y^2 y^2}}$$

The conic constants k_x and k_y; and curvatures c_x and c_y (inverse of radius of curvature) were obtained from a least square fitting (Wolfram Mathematica software) of the Pentacam corneal elevation data to a biconic surface. Coefficients of determination (R^2) of fits were always higher than 0.996 for both anterior/posterior corneal surfaces.

Central corneal thickness was also obtained from the Pentacam data. Corneal and humors refractive indeces were adopted from the Liou-Brennan eye model [12].

The retinal surface z-coordinate for the horizontal meridian was obtained using linear interpolation of the elevation data. Similar to corneal topography, "*elevation*" means sagittal height in relation to a reference plane perpendicular to the optical axis. It was obtained after conversion of the Lenstar AXL data into sag (elevation) data using the equations by Verkicharla et al. [35]. Retinal "elevation" data were then incorporated into Zemax as a "grid sag" surface. Horizontal retinal profile data were stored in a vector of 65 elevation points equally spaced by steps of 0.25 mm. The axial distances between optical elements (cornea, lens and retina) were all obtained from the Lenstar data.

The lens model was obtained as an individualized version of the Liou-Brennan average lens model [12], re-calculated after on-axis optimization of certain lens variables as described below, to fit experimental on-axis refraction and aberrations. The starting point of the optimization was the average Liu-Brennan lens model, but with a modified thickness according to the lens thickness data measured by the Lenstar. Because the Liou-Brennan lens model has an asymmetric variation of the axial refractive index, the actual model was also split in these two axial parts according to the original Liou-Brennan lens model ratio (40% of total lens thickness split to the anterior part and 60% to the posterior part). The axial quadratic polynomial variation of the refractive index was made constant for all subjects. However, the radial rotationally symmetric variation of the refractive index was made variable, allowing up to a sixth order radial polynomial change (coefficients of second, fourth and sixth order were made variables for an optimization procedure). Curvatures and conic constant of anterior and posterior lens surfaces were also made variables. To fit lens astigmatism, the posterior lens surface was introduced in Zemax as an "irregular" surface, which allows modifying the astigmatic coefficient (cylinder and axis of the lens surface) during the optimization procedure. The target merit function consisted of the combination of the equally weighted measured Hartmann-Shack on-axis coefficients of defocus, astigmatism, fourth order spherical aberration and sixth order spherical aberration. After running the optimization procedure (Zemax dampened least squared algorithm) for the lens, an individualized eye model capable of reproducing the on-axis optical quality was generated. The radially symmetric gradient refractive index of these models is shown in Fig. 1 (red lines) and compared to values from the literature [36,37].

For every eye model built, the field angle was changed between -20 and 20 degrees (1 degree step) and peripheral aberrations (low and higher order aberrations) for a 4 mm pupil diameter were obtained from Zemax software as a function of the field angle. The refractive profiles were then compared to those measured by the peripheral Hartmann-Shack wavefront sensor. Figure 2 shows a Zemax ray-tracing layout obtained for one myopic subject with ray bundles at ±20°, ± 12° and 0° field angles.
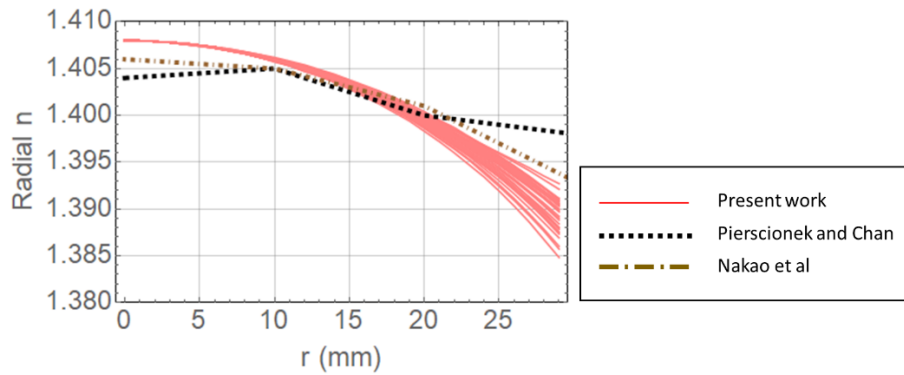
Fig. 1. Radial refractive index as a function of the radial lens coordinate at the equatorial plane of the lens. Red lines represent the lens models obtained after optimization of the initial Liou-Brennan values.
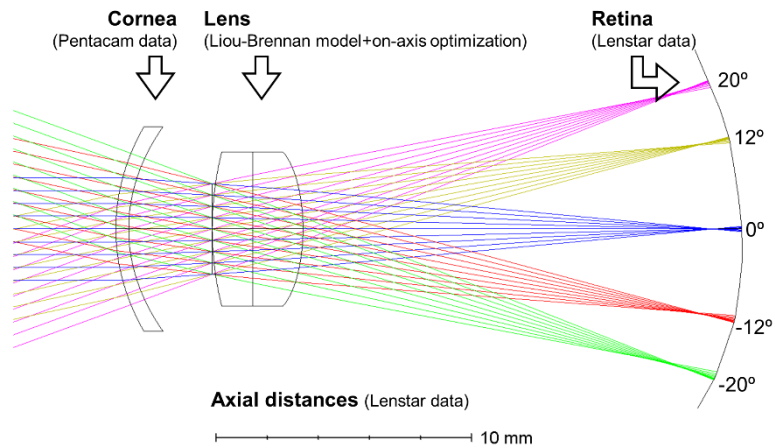

Fig. 2. Zemax customized eye model layout. Notice the myopia of these particular subject as the rays focus in front of the retina.

2.3. Subjects

Young healthy subjects (n = 25, mean age 23.88 ± 1.42 years) with a range of refractive error (spherical equivalent, SE, of the right eye) between +0.13 and -11.38D (mean -3.41 ± 3.32D) and on-axis AXL between 22.66 and 29.42 mm (mean 24.63 ± 1.63 mm) participated in the study. Only data from the right eyes were used in the analyses. The study procedures followed the tenets of the Declaration of Helsinki and were approved by the NECO institutional review board (IRB). After the experiments and procedures were explained and any questions had been answered, the informed consent form was signed by the subjects.

3. Results

Figure 3 shows a one-by-one comparison of relative-to-center defocus between the peripheral Hartmann-Shack sensor data and the prediction of the personal model for each subject. Defocus values were obtained after converting the fourth Zernike coefficient (Z4) into diopters (mean spherical equivalent) [38]. The abrupt myopic peak that tended to show up on the positive side of the eccentricity values represented the optic nerve excavation on the nasal retina. In general, a

large variability of the defocus profiles and the inter-individual tendencies were well captured by the models.
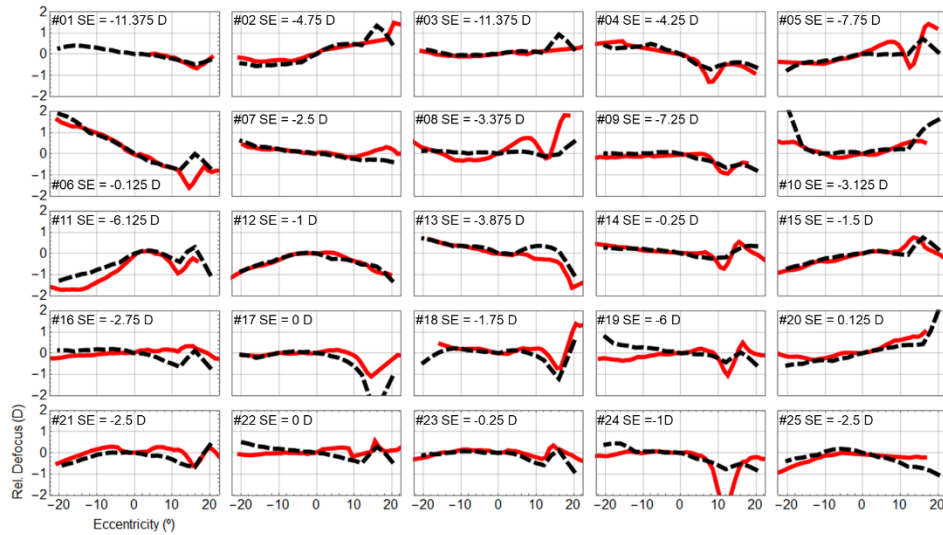

Fig. 3. Comparison of relative peripheral defocus between Hartmann-Shack measurements (red lines) and modelling (black-dashed lines) as a function of field eccentricity for the 25 participants. Negative angle values indicate Nasal fields (object space) and Positive angles indicate Temporal fields.

Figure 4 shows a Bland-Altman plot (differences between predicted and measured values plotted against the mean value) at three eccentricities (10, 15 and 20 degrees). The mean differences between the predicted and the measured value and the interval between the limits of agreement (Mean ± 1.96SD) (expressed on the format [mean, interval of agreement]) were [+0.09, 0.75] D; [+0.10, 0.96] D and [+0.24, 1.85] D for 10, 15 and 20 degrees of eccentricity respectively.
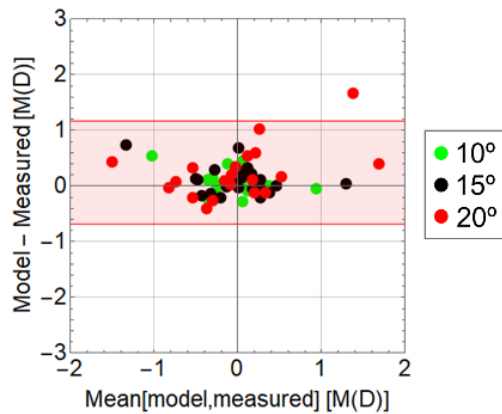

Fig. 4. Bland-Altman plot comparing the difference between model and measured values with the average of these values, shaded area in red shows the limits of agreement for the 20-degree data.

Astigmatism is also expected to change as a function of the angle of eccentricity. Since aberrometry measurements were taken along the horizontal meridian, it was expected that the J0 component will change quadratically as a function of the horizontal angle of eccentricity. Regarding J45, no significant changes as a function of eccentricity were measured. Figure 5 shows the overall comparison of relative to center astigmatism (J0 component) between predicted and measured values. As expected from theory, the change of astigmatism against the angle of eccentricity followed a parabolic profile [39]. In general, the measured and predicted relative astigmatic parabolas had very similar profiles.
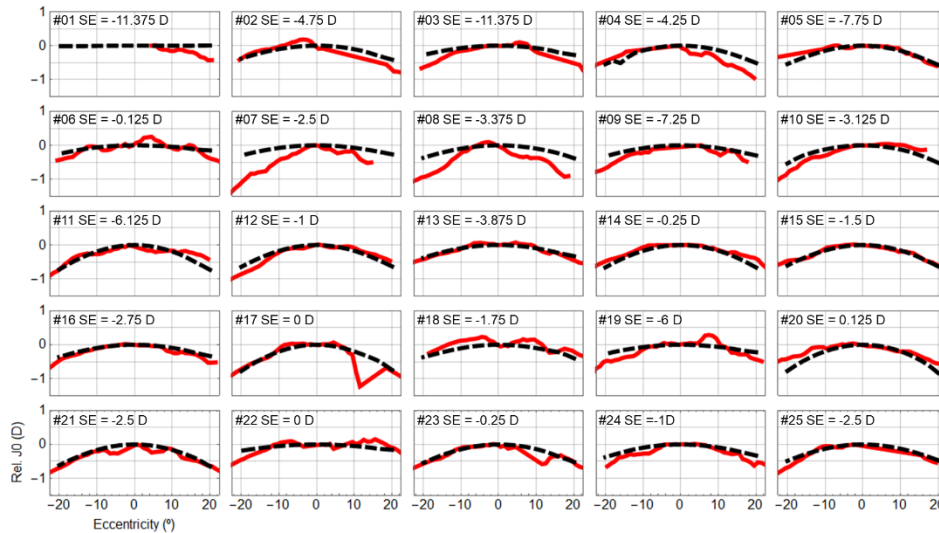

Fig. 5. Comparison of relative astigmatism (J0 component) between Hartmann-Shack measurements (red) and modelling (black-dashed) as a function of field eccentricity for the 25 participants. Negative angle values indicate Nasal fields (object space) and Positive angles indicate Temporal fields.

The differences between the measured data and models were very small (and randomly oriented), as shown by Bland-Altman plots in Fig. 6. Mean differences between the predicted and the measured value and the interval of confidence (same format as for relative defocus) were [0.00, 0.48] D; [+0.09, 0.74] D and [+0.13, 1.00] D for 10, 15 and 20 degrees of eccentricity respectively.

Beyond defocus and astigmatism, the aberration of coma shows a theoretical linear relationship with the eccentricity angle [39]. The theoretical linearity was also well reproduced by our model, but in this case the models tended to overestimate coma compared to the actual measured values (pupil diameter was 4 mm). The differences, shown by the Bland-Altman plot (Fig. 7), and the intervals of confidence were [-0.10, 0.28] μm; [-0.11, 0.41] μm and [-0.15, 0.44] μm for 10, 15 and 20 degrees of eccentricity respectively.

While the disagreement in coma values may be relatively important, in practical and absolute terms it was a very small bias compared to more heavy weighted Zernike terms induced in the periphery, such as off-axis defocus and astigmatism. Coma is even less important for our myopic subjects where strong on-axis defocus was already present. In order to show the influence of the coma disagreement on peripheral imaging, the Point Spread Function (PSF) of one of the *less* myopic subjects in the study (#24, SE -1.00D) was calculated at 20 degrees using the Zernike coefficients measured with the scanning Hartmann-Shack. Also, the extended retinal image was estimated from the convolution of the PSF with an object, in this case a letter F subtending 0.5
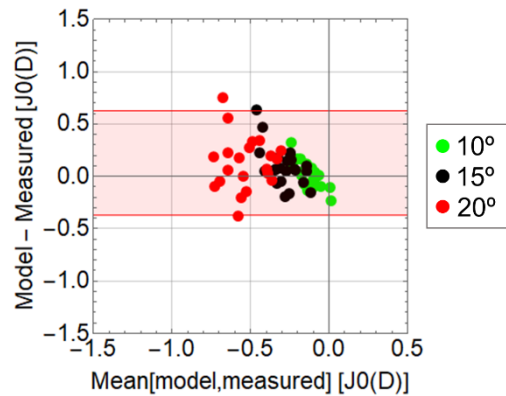
Fig. 6. Bland-Altman plot for Astigmatism (J0). Shaded area in red shows the limits of agreement for the 20-degree data.
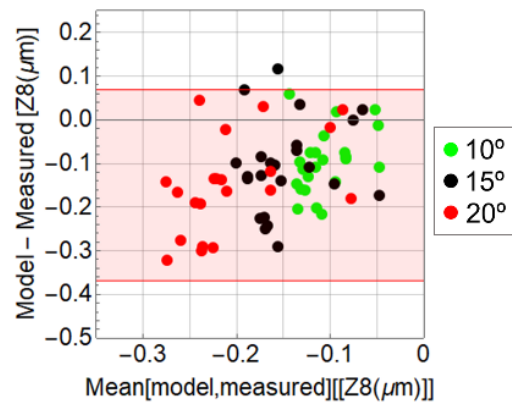

Fig. 7. Bland-Altman plot for horizontal coma. Shaded area in red shows the limits of agreement for the 20-degree data.
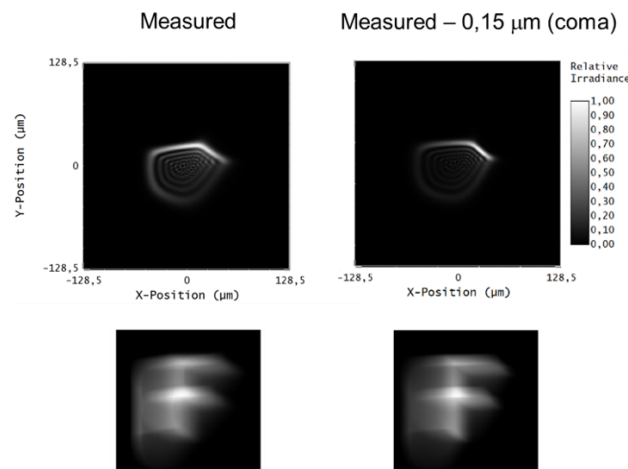

Fig. 8. Point Spread Function (PSF) measured at 20 degrees of eccentricity for subject #24 and the corresponding calculated retinal image of an object (letter F, object size is a square of 0.5 degrees wide). PSF and image on the right represents the same calculation but subtracting -0.15 mm of coma.

degrees height. The same calculations were repeated after subtracting 0.15 μm to the Zernike coma term (the average disagreement error at 20 degrees). Figure 8 shows the results of both calculations, only very subtle changes are appreciated on the PSFs and retinal images. The differences are even smaller at angles closer to the center.

4. Discussion

This study demonstrates that individual predictions of peripheral optical properties of the eye are possible using accurate central aberration data plus corneal surface data, axial distances, and a model for the retinal surface. All these measurements are possible in a clinical setting. It is important to note that this approach was essentially different to other recent attempts to create customized wide-angle eye models in that we did not try to solve a complete inverse problem from peripheral data using a huge computational workload [19,40]; neither did we optimize the retinal surface to fit the expected refractive outcome [41]. Instead, from measured central aberration data and a custom model for the cornea and retinal surfaces, we built models of peripheral optics that were validated using measured peripheral wavefront data. The procedure was relatively simple and generated eye models with an anatomical retinal shape based on real measurements.

The retinal surface was the most critical component of the system. The use of retinal surfaces based on actual experimental measures provided an advantage compared to the use of spheres or conicoids which are just mathematical surfaces fitted to data. However, using these surfaces presented some difficulties and limitations. First, they were not obtained from a single and quick measurement but required a set of AXL measurements to sample the retina field space. This was time-consuming and some subjects may not have accurately fixated on the off-axis targets for all locations. Also, technical limitations may arise when only a limited sample density is available. Here, we chose a compromise between sampling density and an acceptable time for measurements. Another limitation of this method was the intrinsic optimization of optical biometers to perform on-axis measurements and the need for conversion between AXL into sag coordinates [42]. This procedure is not exact and required to take approximations from modelling [35]. Finally, these measurements were taken mostly from myopic eyes, whose retinal surface may be more irregular than in emmetropic eyes [43]. These potential irregularities may have generated a bumpier retinal surface that could be more affected by a limited sampling density.

Our model was accurate in the characterization of optical properties over a central field of 40 degrees. Ideally, the farther we could go into the periphery, the better. However, we were limited by the retinal surface, as the accuracy of the optical biometer decreases with the eccentricity of the measurements. In fact, it was observed that the accuracy of the model, particularly of coma (Fig. 7), starts to decrease at 20 degrees eccentricity. Liu and Thibos [40], using a more complex procedure, were able to build their customized models only up to 30 degrees central field. Our model reaches larger eccentricities (40 degrees central field) to visualize and characterize the typical variability of relative peripheral refraction profiles (Fig. 3). To our knowledge, there are no better alternatives to get more peripheral zones of the retina. Magnetic resonance imaging (MRI) provides a full image of the eye globe, but these images are noisier and contain significantly more uncertainty [35] than the method used here.

Even with these limitations, the prediction of relative peripheral optical quality (defocus and the J0 component of astigmatism) was generally very good. The mean differences at different eccentricities were all well under 0.25 D and with no significant bias (Bland-Altmann plots). However, coma was slightly biased towards more negative predicted values. Still, even for coma the highest mean difference was -0.15 μm, which was a smaller value than the roughly 0.2 μm of RMS error obtained from the fully adjusted models of Liu and Thibos [40] and Goncharev et al. [19]. Besides, this error hardly had any implication in the retinal image and was clearly diluted by the much stronger low order refractive errors on the retina (Fig. 8). The origin of the bias could be in part generated by a tilt and/or decentration of the crystalline lens [44,45], which was

not included here to avoid extra variables on the lens optimization procedure and keep the model as simple as possible.

Individualized eye modelling for myopic eyes can be very relevant for the design of new optical corrections aiming to stop the progression of myopia. It is known that peripheral refractions present a high variability even in myopes [46]. Here, we also demonstrate a large amount of variability in defocus and astigmatism (see the different profiles in Figs. 3 and 5). Lenses designed to control the progression of myopia [25] generally aim to impose a relative peripheral myopic refractive error on the retina. Given the variability of peripheral aberrations, customization of the peripheral profile of ophthalmic lenses would not only make the effect of optical solutions (contact or spectacle lenses) more homogenous across the population but would also likely increase the rate of success of these treatments. In this context, these models will be an ideal tool for the optical design of such myopic corrections.

In conclusion, this study presents a simple and effective procedure to generate peripheral eye models that accurately reproduce the individual optical quality of myopic eyes over a central field of 40 degrees. Given the established individual variability of peripheral aberrations in myopia, these models represent the perfect personalized platform to design new optical treatments to control the progression of myopia.

Disclosures. The authors declare no conflicts of interest.

Data availability. Data of this paper are not publicly available, but it may be obtained from the corresponding author upon reasonable request.

References

1. B. Ehinger and A. Grzybowski, "Allvar Gullstrand (1862-1930)–the gentleman with the lamp," Acta Ophthalmol. **89**(8), 701–708 (2011).
2. H. H. Emsley, *Visual Optics* (Hatton Press, 1955).
3. H. von Helmholtz, *Helmholtz's Treatise on Physiological Optics*, (Optical Society of America, 1924).
4. Y. LeGrand and S. G. ElHage, *Physiological Optics* (Springer, 1980).
5. M. H. E. Tscherning, *Physiologic Optics* (Keystone Pub. Co., 1924).
6. W. Lotmar, "Theoretical eye model with aspherics*," J. Opt. Soc. Am. **61**(11), 1522–1529 (1971).
7. N. Drasdo and C. W. Fowler, "Non-linear projection of the retinal image in a wide-angle schematic eye," Br. J. Ophthalmol. **58**(8), 709–714 (1974).
8. A. C. Kooijman, "Light distribution on the retina of a wide-angle theoretical eye," J. Opt. Soc. Am. **73**(11), 1544–1550 (1983).
9. O. Pomerantzeff, M. Pankratov, G. J. Wang, and P. Dufault, "Wide-angle optical model of the eye," Am. J. Optom. Physiol. Opt. **61**(3), 166–176 (1984).
10. R. Navarro, J. Santamaría, and J. Bescós, "Accommodation-dependent model of the human eye with aspherics," J. Opt. Soc. Am. A **2**(8), 1273–1281 (1985).
11. L. N. Thibos, M. Ye, X. Zhang, and A. Bradley, "The chromatic eye: a new reduced-eye model of ocular chromatic aberration in humans," Appl. Opt. **31**(19), 3594–3600 (1992).
12. H. L. Liou and N. A. Brennan, "Anatomically accurate, finite model eye for optical modeling," J. Opt. Soc. Am. A **14**(8), 1684–1695 (1997).
13. I. Escudero-Sanz and R. Navarro, "Off-axis aberrations of a wide-angle schematic eye model," J. Opt. Soc. Am. A **16**(8), 1881–1891 (1999).
14. D. Siedlecki, H. Kasprzak, and B. K. Pierscionek, "Schematic eye with a gradient-index lens and aspheric surfaces," Opt. Lett. **29**(11), 1197–1199 (2004).
15. A. V. Goncharov and C. Dainty, "Wide-field schematic eye models with gradient-index lens," J. Opt. Soc. Am. A **24**(8), 2157–2174 (2007).
16. J. J. Rozema, P. Rodriguez, R. Navarro, and M.-J. Tassignon, "SyntEyes: a higher-order statistical eye model for healthy eyes," Invest. Ophthalmol. Visual Sci. **57**(2), 683–691 (2016).

17. P. K. Verkicharla, A. Mathur, E. A. Mallen, J. M. Pope, and D. A. Atchison, "Eye shape and retinal shape, and their relation to peripheral refraction," Ophthalmic Physiol. Opt. J. Br. Coll. Ophthalmic Opt. Optom. **32**(3), 184–199 (2012).

18. J. Polans, B. Jaeken, R. P. McNabb, P. Artal, and J. A. Izatt, "Wide-field optical model of the human eye with asymmetrically tilted and decentered lens that reproduces measured ocular aberrations," Optica **2**(2), 124 (2015).

19. A. V. Goncharov, M. Nowakowski, M. T. Sheehan, and C. Dainty, "Reconstruction of the optical system of the human eye with reverse ray-tracing," Opt. Express **16**(3), 1692–1703 (2008).

20. D. O. Mutti, R. I. Sholtz, N. E. Friedman, and K. Zadnik, "Peripheral refraction and ocular shape in children," Invest. Ophthalmol. Visual Sci. **41**(5), 1022–1030 (2000).

21. A. Seidemann, F. Schaeffel, A. Guirao, N. Lopez-Gil, and P. Artal, "Peripheral refractive errors in myopic, emmetropic, and hyperopic young subjects," J. Opt. Soc. Am. A **19**(12), 2363–2373 (2002).

22. D. O. Mutti, J. R. Hayes, G. L. Mitchell, L. A. Jones, M. L. Moeschberger, S. A. Cotter, R. N. Kleinstein, R. E. Manny, J. D. Twelker, and K. Zadnik, and CLEERE Study Group, "Refractive error, axial length, and relative peripheral refractive error before and after the onset of myopia," Invest. Ophthalmol. Visual Sci. **48**(6), 2510–2519 (2007).

23. J. Wallman and J. Winawer, "Homeostasis of eye growth and the question of myopia," Neuron **43**(4), 447–468 (2004).

24. E. L. Smith, C.-S. Kee, R. Ramamirtham, Y. Qiao-Grider, and L.-F. Hung, "Peripheral vision can influence eye growth and refractive development in infant monkeys," Invest. Ophthalmol. Visual Sci. **46**(11), 3965–3972 (2005).

25. N. S. Anstice and J. R. Phillips, "Effect of dual-focus soft contact lens wear on axial myopia progression in children," Ophthalmology **118**(6), 1152–1161 (2011).

26. C. Chen, S. W. Cheung, and P. Cho, "Myopia Control Using Toric Orthokeratology (TO-SEE Study)," Invest. Ophthalmol. Visual Sci. **54**(10), 6510 (2013).

27. J. Tabernero, D. Vazquez, A. Seidemann, D. Uttenweiler, and F. Schaeffel, "Effects of myopic spectacle correction and radial refractive gradient spectacles on peripheral refraction," Vision Res. **49**(17), 2176–2186 (2009).

28. D. A. Atchison, "Optical models for human myopic eyes," Vision Res. **46**(14), 2236–2250 (2006).

29. J. Tabernero, "Customized eye models," in *Handbook of Visual Optics, Volume One* (CRC Press, 2017).

30. J. Tabernero, P. Piers, A. Benito, M. Redondo, and P. Artal, "Predicting the optical performance of eyes implanted with IOLs to correct spherical aberration," Invest. Ophthalmol. Visual Sci. **47**(10), 4651–4658 (2006).

31. P. Rosales and S. Marcos, "Customized computer models of eyes with intraocular lenses," Opt. Express **15**(5), 2204–2218 (2007).

32. B. Jaeken, L. Lundström, and P. Artal, "Fast scanning peripheral wave-front sensor for the human eye," Opt. Express **19**(8), 7903–7913 (2011).

33. E. J. Fernandez, S. Sager, Z. Lin, J. Hao, J. Roca, P. M. Prieto, Z. Yang, W. Lan, and P. Artal, "Instrument for fast whole-field peripheral refraction in the human eye," Biomed. Opt. Express **13**(5), 2947 (2022).

34. C. McAlinden, J. Khadka, and K. Pesudovs, "A comprehensive evaluation of the precision (repeatability and reproducibility) of the Oculus Pentacam HR," Invest. Ophthalmol. Visual Sci. **52**(10), 7731–7737 (2011).

35. P. K. Verkicharla, M. Suheimat, J. M. Pope, F. Sepehrband, A. Mathur, K. L. Schmid, and D. A. Atchison, "Validation of a partial coherence interferometry method for estimating retinal shape," Biomed. Opt. Express **6**(9), 3235–3247 (2015).

36. B. K. Pierscionek and D. Y. Chan, "Refractive index gradient of human lenses," Optom. Vis. Sci. Off. Publ. Am. Acad. Optom. **66**(12), 822–829 (1989).

37. S. Nakao and T. Ono, "[Refractive index distribution in the primate crystalline lens and its schematic eye]," Nihon Ganka Kiyo **20**, 533–536 (1969).

38. L. N. Thibos, X. Hong, A. Bradley, and R. A. Applegate, "Accuracy and precision of objective refraction from wavefront aberrations," J. Vis. **4**(4), 9–351 (2004).

39. L. N. Hazra and C. A. Delisle, "Primary aberrations of a thin lens with different object and image space media," J. Opt. Soc. Am. A **15**(4), 945–953 (1998).

40. T. Liu and L. N. Thibos, "Customized models of ocular aberrations across the visual field during accommodation," J. Vis. **19**(9), 13 (2019).

41. Q. Li and F. Fang, "Retinal contour modelling to reproduce two-dimensional peripheral spherical equivalent refraction," Biomed. Opt. Express **12**(7), 3948–3964 (2021).

42. D. A. Atchison and J. J. Rozema, "Technical notes on peripheral refraction, peripheral eye length and retinal shape determination," Ophthalmic Physiol. Opt. **43**(3), 584–594 (2023).

43. J. Tabernero and F. Schaeffel, "More irregular eye shape in low myopia than in emmetropia," Invest. Ophthalmol. Visual Sci. **50**(9), 4516–4522 (2009).

44. E. Berrio, J. Tabernero, and P. Artal, "Optical aberrations and alignment of the eye with age," J. Vis. **10**(14), 34 (2010).

45. J. Tabernero, A. Benito, E. Alcón, and P. Artal, "Mechanism of compensation of aberrations in the human eye," J. Opt. Soc. Am. A **24**(10), 3274–3283 (2007).

46. J. Tabernero, A. Ohlendorf, M. D. Fischer, A. R. Bruckmann, U. Schiefer, and F. Schaeffel, "Peripheral refraction profiles in subjects with low foveal refractive errors," Optom. Vis. Sci. Off. Publ. Am. Acad. Optom. **88**(3), E388–E394 (2011).